Milliarcsecond localization of the hyperactive repeating FRB 20220912A

Citation for the original published paper (version of record):
Hewitt, D., Bhandari, S., Marcote, B. et al (2024). Milliarcsecond localization of the hyperactive repeating FRB 20220912A. Monthly Notices of the Royal Astronomical Society, 529(2): 1814-1826. http://dx.doi.org/10.1093/mnras/stae632

Monthly Notices of the ROYAL ASTRONOMICAL SOCIETY

MNRAS **529,** 1814–1826 (2024) https://doi.org/10.1093/mnras/stae632
Advance Access publication 2024 March 05

Milliarcsecond localization of the hyperactive repeating FRB 20220912A

Danté M. Hewitt [1]★ Shivani Bhandari [1,2,3,4] Benito Marcote [3] Jason W. T. Hessels,[1,2] Kenzie Nimmo [5] Franz Kirsten,[6] Uwe Bach [7] Vladislavs Bezrukovs,[8] Mohit Bhardwaj,[9] Richard Blaauw,[2] Justin D. Bray,[10] Salvatore Buttaccio,[11] Alessandro Corongiu [12] Marcin P. Gawroński,[13] Marcello Giroletti [11] Aard Keimpema,[3] Giuseppe M. Maccaferri,[11] Zsolt Paragi [3] Matteo Trudu,[12] Mark P. Snelders,[1,2] Tiziana Venturi,[11] Na Wang,[14] David R. A. Williams-Baldwin [10] Nicholas H. Wrigley [10] Jun Yang [6] and Jianping P. Yuan[14]

[1]*Anton Pannekoek Institute for Astronomy, University of Amsterdam, Science Park 904, NL-1098 XH Amsterdam, the Netherlands*
[2]*ASTRON, Netherlands Institute for Radio Astronomy, Oude Hoogeveensedijk 4, NL-7991 PD Dwingeloo, the Netherlands*
[3]*Joint Institute for VLBI ERIC, Oude Hoogeveensedijk 4, NL-7991 PD Dwingeloo, the Netherlands*
[4]*CSIRO Space and Astronomy, Australia Telescope National Facility, PO Box 76, Epping, NSW 1710, Australia*
[5]*MIT Kavli Institute for Astrophysics and Space Research, Massachusetts Institute of Technology, 77 Massachusetts Ave, Cambridge, MA 02139, USA*
[6]*Department of Space, Earth and Environment, Chalmers University of Technology, Onsala Space Observatory, SE-439 92 Onsala, Sweden*
[7]*Max-Planck-Institut für Radioastronomie, Auf dem Hügel 69, D-53121 Bonn, Germany*
[8]*Engineering Research Institute Ventspils International Radio Astronomy Centre of Ventspils University of Applied Sciences, Inženieru street 101, Ventspils LV-3601, Latvia*
[9]*McWilliams Center for Cosmology, Department of Physics, Carnegie Mellon University, Pittsburgh, PA 15213, USA*
[10]*Jodrell Bank Centre for Astrophysics, Department of Physics and Astronomy, The University of Manchester, Manchester M13 9PL, UK*
[11]*INAF – Istituto di Radioastronomia, Via Gobetti 101, I-40129 Bologna, Italy*
[12]*INAF – Osservatorio Astronomico di Cagliari, via della Scienza 5, I-09047 Selargius (CA), Italy*
[13]*Institute of Astronomy, Faculty of Physics, Astronomy and Informatics, Nicolaus Copernicus University, Grudziadzka 5, PL-87-100 Toruń, Poland*
[14]*Xinjiang Astronomical Observatory, CAS, 150 Science 1-Street, Urumqi, Xinjiang 830011, China*

Accepted 2024 February 26. Received 2024 February 20; in original form 2023 December 22

ABSTRACT

We present very long-baseline interferometry (VLBI) observations of the hyperactive repeating FRB 20220912A using the European VLBI Network (EVN) outside of regular observing sessions (EVN-Lite). We detected 150 bursts from FRB 20220912A over two observing epochs in 2022 October. Combining the burst data allows us to localize FRB 20220912A to a precision of a few milliarcseconds, corresponding to a transverse scale of less than 10 pc at the distance of the source. This precise localization shows that FRB 20220912A lies closer to the centre of its host galaxy than previously found, although still significantly offset from the host galaxy's nucleus. On arcsecond scales, FRB 20220912A is coincident with a persistent continuum radio source known from archival observations; however, we find no compact persistent emission on milliarcsecond scales. The 5σ upper limit on the presence of such a compact persistent radio source is 120 μJy, corresponding to a luminosity limit of $(\mathrm{D}/362.4\,\mathrm{Mpc})^2\ 1.8 \times 10^{28}\mathrm{erg\,s^{-1}\,Hz^{-1}}$. The persistent radio emission is thus likely to be from star formation in the host galaxy. This is in contrast to some other active FRBs, such as FRB 20121102A and FRB 20190520B.

Key words: techniques: high angular resolution – radio continuum: transients – fast radio bursts.

1 INTRODUCTION

Fast radio bursts (FRBs) are flashes of coherent radio emission that have durations of microseconds to seconds (for a recent review see Petroff, Hessels & Lorimer 2022). Some of them are known to repeat (Spitler et al. 2016). While more than 2000 unique sources of FRBs have been detected to date (Chime/Frb Collaboration 2023), fewer than 50 have been localized to a host galaxy.[1] Precise localizations of FRBs are key to understanding their origins and for using them as astrophysical and cosmological probes. While arcsecond precision is normally sufficient to identify a host galaxy robustly (Eftekhari & Berger 2017), subarcsecond localizations are key to identifying the specific galactic and stellar neighbourhoods in which FRB sources reside (e.g. Tendulkar et al. 2021).

★ E-mail: d.m.hewitt@uva.nl

[1]The FRB Community Newlsetter (Vol. 4, Issue 12, DOI: 10.7298/X3BX-0E49) reported 44 host galaxies.

Magnetars are widely favoured as the engines powering FRBs, given the high burst rate and millisecond time-scales associated with some FRBs (e.g. Ravi 2019; Li et al. 2021; Nimmo et al. 2021), as well as the detection of exceptionally bright radio bursts from the Galactic magnetar SGR 1935+2154 that were coincident with an X-ray burst (Bochenek et al. 2020; CHIME/FRB Collaboration 2020). Nonetheless, the diverse properties and environments of FRB sources suggest that a single magnetar progenitor model may be overly simplistic (e.g. Kirsten et al. 2022a).

FRB sources show a wide range of repetition rates, from a few hyperactive repeaters[2] to apparent one-off events that constitute 97 per cent of the currently known sources (Chime/Frb Collaboration 2023). The lack of obvious bimodality in the burst rates suggests that one-off sources may be capable of repeating (Chime/Frb Collaboration 2023), but statistically significant differences in burst properties between repeaters and non-repeaters suggest they may be distinct (Pleunis et al. 2021). Another possibility is that a single source model is capable of producing multiple burst types (Hewitt et al. 2023; Snelders et al. 2023). Both repeaters and (apparent) non-repeaters have been localized to a wide variety of host galaxies, with no clear distinction in galaxy type (Bhardwaj et al. 2023; Gordon et al. 2023). There is an overall trend towards star-forming galaxies, with notable exceptions (Sharma et al. 2023).

The global galactic properties of an FRB host are only indirectly informative about the source's nature. More directly, we can study the local environment of FRB sources via time-variable propagation effects (e.g. Michilli et al. 2018) and precision localization coupled to high-resolution imaging (e.g. Mannings et al. 2021). Ideally, radio localizations should have <100 mas uncertainty, in order to maximize the degree to which one can zoom-in on their local environment. Thus far, only five repeaters, and as yet no non-repeaters, have been localized to milliarcsecond precision (Marcote et al. 2017, 2020; Nimmo et al. 2022; Kirsten et al. 2022a; Bhandari et al. 2023).

The first detected repeater, FRB 20121102A, was localized to a low-metallicity star-forming dwarf galaxy (Chatterjee et al. 2017; Tendulkar et al. 2017). These observations also showed that FRB 20121102A was spatially consistent with a faint compact persistent radio source (PRS). Follow-up observations by the EVN (European VLBI Network; Marcote et al. 2017) enabled milliarcsecond localization of the bursts and concrete association between the bursts and PRS (a projected linear separation of $\lesssim$40 pc). Marcote et al. (2017) also showed that the PRS is compact on sub-parsec scales, and hence cannot be due to local star formation. Rather, it may be a hyper-nebula powered by the FRB source, or a low luminosity active galactic nucleus (Marcote et al. 2017). The precision of this FRB 20121102A localization further enabled characterization of the local environment using the *Hubble Space Telescope* (*HST*; Bassa et al. 2017), which revealed that FRB 20121102A is spatially coincident, but slightly off centre ($\sim$200 pc) from a knot of star formation in its host galaxy. Together with the source's extreme and highly variable Faraday rotation measure (RM; Michilli et al. 2018), this supports the case for a young magnetar progenitor (e.g. Metzger, Margalit & Sironi 2019).

Thereafter, the repeating and periodically active (Chime/Frb Collaboration 2020), FRB 20180916B was localized by the EVN to a nearby massive spiral galaxy (Marcote et al. 2020). The precision of the EVN localization allowed for the association of the FRB source with the apex of a relatively large, apparently ν-shaped star formation region, but also ruled out the presence of a PRS, distinguishing it from the other known and localized repeater at the time. Follow-up *HST* observations showed that FRB 20180916B is located slightly offset ($\sim$250 pc) from the nearest knot of star formation – suggesting that it is a neutron star formed by a runaway massive star, or perhaps an older neutron star in a binary system (Tendulkar et al. 2021).

The hyperactive repeater FRB 20201124A (e.g. Lanman et al. 2022), was first localized to arcsecond precision by the Australian Square Kilometre Array Pathfinder (ASKAP; Day et al. 2021), Very Large Array/realfast (VLA; Law et al. 2021), and upgraded Giant Metrewave Radio Telescope (uGMRT; Wharton et al. 2021b). The host galaxy was found to be star-forming, dusty, and an order of magnitude more massive than the hosts of other repeaters at the time, bridging the gap between the hosts of repeaters and apparent non-repeaters (Ravi et al. 2022). The VLA (in D-configuration) and uGMRT detected unresolved, persistent radio emission at radio frequencies of 3 and 9 GHz (Ricci et al. 2021), and 300 MHz (Wharton et al. 2021a), respectively. Follow-up observations with the VLA (in C-configuration) at 22 GHz, however, resolved this emission, disqualifying it as a compact PRS and showing that the radio emission is more likely due to star formation (Piro et al. 2021). Milliarcsecond localization with the EVN (Nimmo et al. 2022) found no evidence of compact radio emission coincident with the burst position, supporting the notion that the previously detected emission is of extended nature and that FRB 20201124A is embedded in a region of star formation. The milliarcsecond localization also enabled deeper, high resolution radio and optical studies with the VLA and *HST*, respectively, leading to the hypothesis that the FRB source formed *in situ* (Dong et al. 2024). More recently, there has been a claim of a low luminosity PRS detected at 15 GHz (Bruni et al. 2023).

Using the raw voltage data of three bursts, the Canadian Hydrogen Intensity Mapping Experiment FRB project (CHIME/FRB; CHIME/FRB Collaboration 2018) localized FRB 20200120E to the outskirts of the M81 spiral galaxy complex (at a luminosity distance of 3.6 Mpc) with a 90 per cent confidence interval of $\simeq$14 arcmin^2 (Bhardwaj et al. 2021). Follow-up observations by Kirsten et al. (2022a) confirmed that FRB 20200120E is indeed associated with the M81 galactic system and, surprisingly, coincident with a globular cluster. This finding challenged theories that advocate that all FRBs originate from young magnetized neutron stars formed via core collapse SNe (supernovae). If FRB 20200120E is indeed such a magnetized neutron star, alternative formation channels need to be invoked: e.g. formation via binary merger or accretion-induced collapse of a white dwarf (Kremer, Piro & Li 2021).

Finally, FRB 20190520B, discovered by the Five-hundred-meter Aperture Spherical Telescope (FAST), was localized to a dwarf host galaxy at a $z = 0.241$ using the VLA (Niu et al. 2022). VLA observations identified a potential PRS with a flux density of $\sim 200\mu$Jy at 3 GHz. Recent observations with the EVN have confirmed the compact PRS nature by constraining the transverse size of the source to be <9 pc. These observations have also showed that the FRB source and the PRS are consistent with being co-located within $\leq$80 pc – consistent with the hypothesis that a single central engine must power both the bursts and the PRS (Bhandari et al. 2023).

The primary focus of this paper, a hyperactive repeater called FRB 20220912A, was discovered by CHIME/FRB (McKinven & Chime/Frb Collaboration 2022). CHIME/FRB reported a position of RA (J2000): 347.29(4)°, Dec. (J2000): +48.70(3)° (90 per cent

[2]We define hyperactive repeaters as repeaters that show sustained activity for weeks to months, observed by many telescopes in multiple frequency bands, e.g. FRB 20201124A.

uncertainty errors), and a dispersion measure (DM) of 219.46(4) pc cm^{-3} for this source. The FRB position lies somewhat outside of the Galactic plane: $l = 106.1°$, $b = -10.8°$. The expected scattering time-scale from the Galactic interstellar medium (ISM) along this line of sight is a moderate 2.6 μs (at 1 GHz) according to the NE2001 Galactic electron density model (Cordes & Lazio 2002). The Deep Synoptic Array (DSA-110) localized FRB 20220912A to a host galaxy, PSO J347.2702+48.70, at $z = 0.0771(1)$ or a luminosity distance of 362.4(1) Mpc (Ravi et al. 2023). The host galaxy has a stellar mass of approximately 10^{10} $M_\odot$ and a star formation rate of $\gtrsim 0.1\,M_\odot\,yr^{-1}$, making it unremarkable compared to some other known host galaxies of repeaters (Gordon et al. 2023). FRB 20220912A is the most active FRB known to date, with FAST detecting as many as 390 bursts per hour (Zhang et al. 2023). Interestingly, the local environment of the source also appears to be clean, as the RM of the bursts has been stable around zero for a period on the order of months (e.g. Feng et al. 2023; Hewitt et al. 2023; Zhang et al. 2023).

Here, we present the interferometric localization of 150 bursts detected from FRB 20220912A with EVN-Lite[3] observations in 2022 October. Section 2 outlines the technical details of our observations. We describe our search pipeline, localization procedures, and the measurement of burst properties in Section 3. Finally, our main conclusions are presented and placed in the context of other FRBs in Section 4.

2 OBSERVATIONS

We observed FRB 20220912A in three observing runs in 2022 October as part of the ongoing FRB VLBI localization programme called PRECISE (Pinpointing REpeating ChIme Sources with EVN dishes; PI: Kirsten). The first observation (Epoch 1; EVN project code EK051G; PRECISE code PR249A) was conducted on 2022 October 22, 00:00–04:46 UT, and utilized an ad hoc array of 11 EVN and eMERLIN (enhanced Multi Element Remotely Linked Interferometer Network) dishes: Cambridge, Darnhall, Defford, Effelsberg, Knockin, Jodrell Bank Mark II, Medicina, Noto, Pickmere, Toruń, and Westerbork. The second observation (Epoch 2; EK051H; PR247A), was conducted from 2022 October 24 21:00 UT to 2022 October 25 02:00 UT. Westerbork did not participate in the second observation and the array consisted of the remaining 10 dishes from Epoch 1. The third observing run (Epoch 3; PR248A), was conducted from 2022 October 26 23:00 UT to 2022 October 27 04:30 UT. During this run, we used the 11 aforementioned dishes as well as the Onsala 25-m telescope. In the first two observations, we pointed the array to a sky position of RA = $23^{h}09^{m}05\overset{s}{.}49$ Dec. = $+48°42'25\overset{''}{.}6$, which is the position of the initial localization determined using the DSA-110 (Ravi 2022). We note that this position is 5.8″ offset from the final reported DSA-110 position, RA = $23^{h}09^{m}04\overset{s}{.}9$ Dec. = $+48°42'25\overset{''}{.}4$ (Ravi et al. 2023), but still well within the primary beam of all EVN dishes. In Epoch 3, we pointed to the updated DSA-110 position. Observations for Epochs 1 and 2 were carried out at a central frequency of 1.4 GHz with bandwidth ranging from 64–256 MHz for the different antennas, and we recorded dual-polarization raw voltage data in a circular basis with 2-bit sampling at all the participating stations in VDIF (VLBI Data Interchange Format; Whitney et al. 2010) format. The frequency coverage was not identical between individual dishes and is illustrated in Fig. 1. For Epoch 3, we observed with a similar set-up but at higher frequencies (4798–5054 MHz). We provide a more concise overview of Epoch 3 as no bursts were detected during this higher frequency observation (Kirsten et al. 2022b).

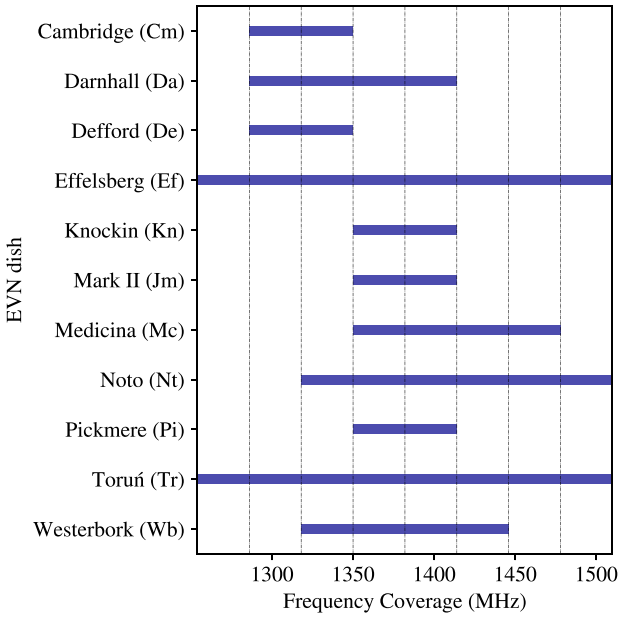

Figure 1. Our PRECISE observations spanned a total bandwidth of 256 MHz from 1254–1510 MHz. The frequency coverage of each of the EVN dishes in the array is shown in the plot by the horizontal bars, while the dashed vertical lines indicate the edges of the sub-bands. Noto observes from 1350–1606 MHz, but only the range below 1510 MHz, where there is overlap with other stations, is correlated.

For Epoch 1, our observations interleaved target scans of 5.75 min on FRB 20220912A and scans of 1.5 min on a nearby (3.0° offset) phase calibrator source, J2311+4543, resulting in phase referencing cycles with a duration of approximately 7.25 min. Every fifth iteration we also observed another nearby source, J2314+4518 (0.6° offset from the phase calibrator), for 3.5 min to be used as an interferometric check source. This check source is used to estimate the absolute astrometric uncertainty and potential amplitude losses that might have been introduced during phase referencing. A 5 min scan was scheduled on J1327+4326 to use as a fringe finder and bandpass calibrator. Finally, the pulsar B2111+46 was also observed for 5 min to verify the integrity of our data for the burst search and single pulse analyses with Effelsberg. A similar strategy was followed in Epochs 2 and 3, but in Epoch 2 the phase calibrator J2311+4543 was also used as a fringe finder and bandpass calibrator, the check source was replaced with J2327+4754 (3.4° offset from the phase calibrator), and B0329+54 was used as a test pulsar. In Epoch 3, we used J2308+4629 as a phase calibrator, J2327+4911 as a check source again (4.1° offset from J2327+4911), J2311+4543 as the fringe finder, and B2020+28 and B0540+23 as test pulsars.

3 ANALYSIS AND RESULTS

3.1 Search for bursts

Inspecting the test pulsar data allowed us to verify that the data quality of our observations was up to par, the bit-mapping was as expected,

[3]EVN-Lite is a new initiative starting in 2023, to address rare/transient phenomena requiring hundreds of hours of observing time with ad hoc subarrays of radio telescopes that form the EVN, outside the regular EVN observing sessions.

and that there were no excessive sources of RFI. We then continued searching the raw voltage data from Effelsberg for bursts, using the pipeline previously described in detail in Kirsten et al. (2021). In short, the raw voltage data were converted to Stokes I filterbanks with time and frequency resolutions of 64 μs and 62.5 kHz, respectively, using DIGIFIL (van Straten & Bailes 2011). We then used the GPU-accelerated transient detection software HEIMDALL[4] to search a DM range of $169 - 269\,\mathrm{pc\,cm^{-3}}$ for FRB candidates that were above a signal-to-noise ratio (S/N) of 7. The resulting candidates were classified by the machine learning convolutional neural network FETCH (Agarwal et al. 2020), using their models 'A' and 'H'.[5] All candidates for which these models assigned a >0.5 probability of the burst being astrophysical in origin were manually inspected. We detected a total of 45 and 105 bursts in the first and second observation, respectively. No bursts were detected in the 5-GHz data from Epoch 3. A subsample of the bursts is shown in Fig. 2.

3.2 Correlation of interferometric data

The PRECISE data were correlated in numerous passes at the Joint Institute for VLBI ERIC (JIVE) in the Netherlands (EVN correlation proposal EK051; PI: Kirsten), making use of the software correlator SFXC (Keimpema et al. 2015). For Epoch 1, the first pass was a delay-mapping correlation where three bursts and their bracketing phase calibrator scans were used to determine the burst position to an uncertainty of ≈1 arcsec (see detailed description in Marcote et al. 2020). The initial DSA-110 localization (Ravi 2022) was used as the phase centre of the FRB 20220912A target field. The correlation was done with 8 × 32 MHz sub-bands consisting of 64 spectral channels each and an integration time of 2 s for the phase calibrator scans, while the target scans were manually gated (temporal selection of the FRB signals to enhance S/N) according to the width of the bursts and coherently dedispersed to a DM of $219.46\,\mathrm{pc\,cm^{-3}}$. In the second pass, all the bursts were coherently dedispersed (dedispersed *within* a channel, as well as with respect to other channels) and correlated at a phase centre determined by the delay-mapping. In order to maximize the S/N, gate widths were chosen around the arrival time of each burst. After the interferometric localization of the FRB 20220912A bursts described in the next section, all target data were then re-correlated in a third and final correlation pass using this position as the phase centre, in order to create a deep image to look for persistent radio continuum counterparts. We repeated the procedure for Epoch 2, but without the first delay-mapping pass (as the position was already known), and using the interferometric localization from Epoch 1 as the phase centre.

During these correlations we encountered a few technical issues that required resolution before finalizing the analysis. The Earth Orientation Parameters (EOPs) used in the correlation of the EK051H data were not properly updated in the correlator due to a failure of a software that pings NASA's Archive of Space Geodesy Data.[6] This was discovered and corrected for the continuum data by re-correlating them with updated EOPs. However, the burst correlation still had outdated EOPs with a large discrepancy, notably in the UT1−UTC values. This initially introduced an offset of ∼30 mas in RA for the position of the burst source between EK051G and EK051H. The offset was resolved internally at JIVE by performing an EOP correction on EK051H burst data. The correction applied a phase shift to the visibilities that corresponds to the delay difference that results from the different sets of parameters. These delays are approximated by using the IAU2000A precession and nutation model to calculate the celestial to terrestrial coordinate transformation matrix. The source code for this implementation is available online[7], and this feature will be added to CASA (McMullin et al. 2007; van Bemmel et al. 2022) in a future release.

3.3 Burst localization

The EVN data were calibrated using standard interferometric techniques in AIPS (Greisen 2003) and DIFMAP (Shepherd, Pearson & Taylor 1994). Imaging was performed in DIFMAP and CASA v6.1.

After the correlated visibilities (in FITS–IDI format) were loaded into AIPS, we first applied the calibration table from the EVN AIPS pipeline that contains the parallactic angle correction and a priori gain correction, using the gain curves and system temperature measurements that the stations recorded during the observations. We also applied the a priori flagging table and bandpass calibration table. We then flagged the edges of sub-bands (≈15 per cent of the channels in total) and manually flagged data from the fringe finder scans that were contaminated by RFI (radio frequency interference). Ionospheric dispersive delays can have a significant impact on the calibration and localization accuracy at milliarcsecond scales at 1.4 GHz. To mitigate this we made use of the VLBATECR task in AIPS to correct for these delays. The task makes use of maps from the Jet Propulsion Laboratory of the total electron content (TEC) at the different EVN sites during the observations, and compensates for the dispersive delays accordingly. We used the fringe finder scans (J1327+4326 for Epoch 1 and J2311+4543 for Epoch 2), with Effelsberg as the reference antenna, to remove the phase jumps between sub-bands and phase slopes within sub-bands that are introduced because of the different signal paths for individual sub-bands. Next, a global fringe fit was performed to correct the phases of the entire observation for all calibrator sources as a function of both frequency and time. The solutions were manually inspected, and bad solutions were flagged.

Having applied the aforementioned calibration, we imaged the phase calibrator (J2311+4543) and check sources (J2314+4518 for Epoch 1 and J2327+4754 for Epoch 2) in DIFMAP using a cell size of 1 mas in each dimension and a natural weighting scheme (synthesized beam sizes of ≈30 × 40 mas). We were able to reproduce the positions of both check sources to a precision of ≲2 mas compared to the expected positions from 5 GHz maps of the sources in the RFC 2023B catalogue.[8] For J2314+4518 we measure a positional offset of $\Delta\alpha = 0.1$mas and $\Delta\delta = 1.0$ mas, and for J2327+4754, a positional offset of $\Delta\alpha = 1.6$ mas and $\Delta\delta = 1.9$ mas. The expected positions of J2314+4518 and J2327+4754 in the 5 GHz maps have uncertainties of 1.06 and 1.47 mas, respectively. Taking these uncertainties into account, together with the difference in observing frequency, we conclude that our calibration was successful. We factor in these positional offsets when determining the FRB position and conservatively include the statistical uncertainty on the check source positions in the calculation of the final FRB positional uncertainty.

We also performed self-calibration to further improve our calibration solutions. We first imaged and self-calibrated the phase calibrator

[4] https://sourceforge.net/projects/heimdall-astro/

[5] Empirical tests that we ran showed that models A and H performed best in terms of completeness and number of false positives.

[6] https://cddis.nasa.gov/Data_and_Derived_Products/Other_products/IERS_EOPs.html

[7] https://code.jive.eu/kettenis/correct_eops

[8] http://astrogeo.org/sol/rfc/rfc_2023b/rfc_2023b_cat.html

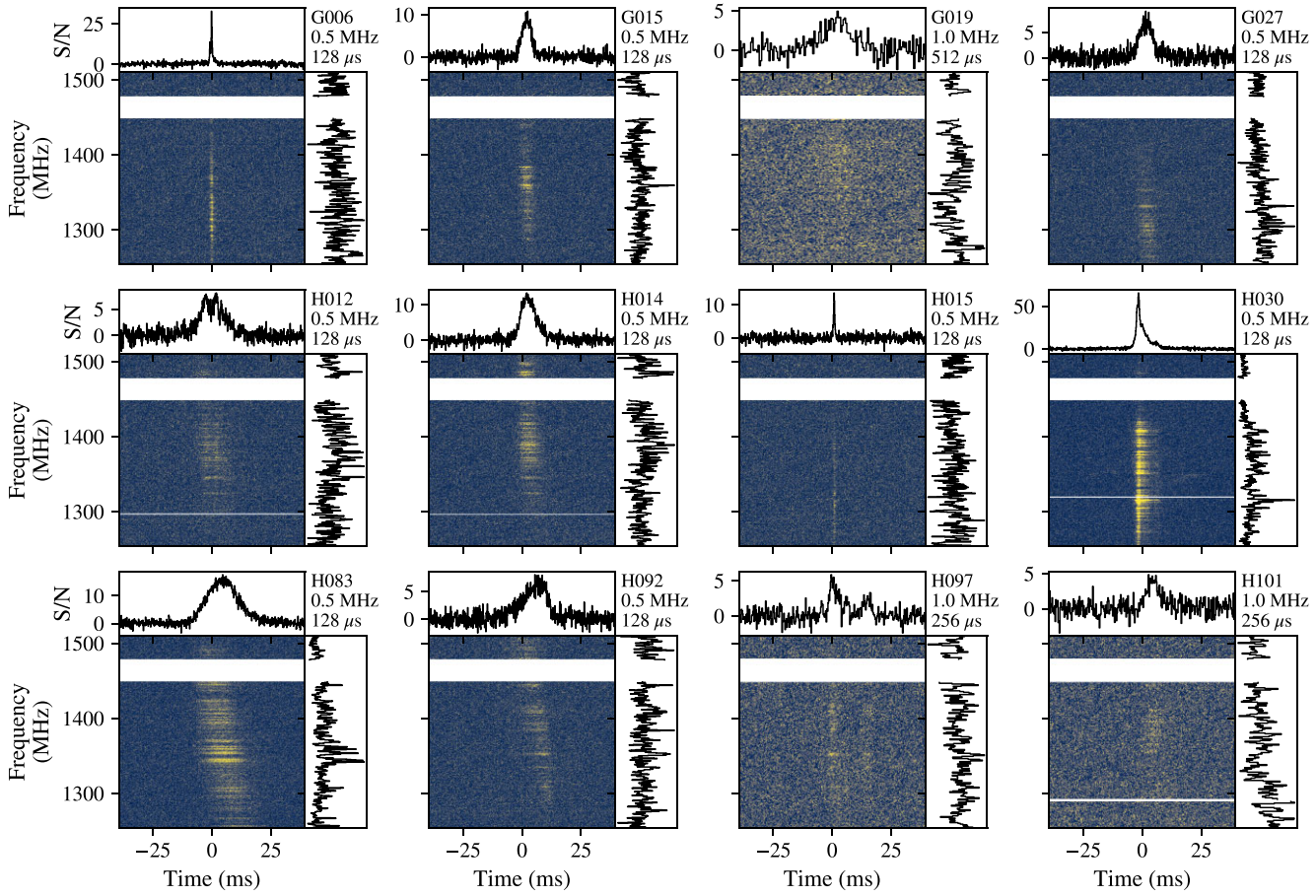

Figure 2. This subsample of bursts detected from FRB 20220912A with the Effelsberg dish illustrates the diversity in burst duration and the complex morphology seen in some high-S/N bursts. All bursts have been dedispersed using a DM of 219.37 pc cm^{-3}. In each thumbnail, the main panel shows the dynamic spectrum of the burst. The top panel shows the frequency-averaged time profile (averaged over the spectral extent of the burst), while the side panel shows the time-averaged frequency spectrum. For visual purposes the bursts have been averaged in time and frequency, and the plotted time and frequency resolutions are shown in the top right corner of each thumbnail, together with the corresponding burst ID in Table A1. Horizontal white lines in the dynamic spectrum indicate channels that have been masked due to the presence of RFI.

in DIFMAP to obtain the best possible model of the source. This model allowed us to improve the phases and amplitudes of the different antennas. The resulting model was imported into AIPS and was used to create a calibration table. Finally, we applied these calibration solutions to the target field of FRB 20220912A and imaged the target (both the continuum data and burst data). We again used a cell size of 1 mas and natural weighting.

We combined the visibilities of the 45 bursts detected in Epoch 1 and 105 bursts detected in Epoch 2 to create the dirty maps shown in Fig. 3 with CASA. In doing so, we assume that all of the bursts are coming from the same unresolved region. Taking into account the positional offset of our check sources, for Epoch 1 we find the position of the bursts from FRB 20220912A to be RA (J2000) = $23^{\rm h}09^{\rm m}04\overset{\rm s}{.}8990 \pm 3.4$ mas, Dec. (J2000) = $48^\circ42'23\overset{''}{.}9104 \pm 3.3$ mas. For Epoch 2, we find a position of RA (J2000) = $23^{\rm h}09^{\rm m}04\overset{\rm s}{.}8987 \pm 3.5$ mas, Dec. (J2000) = $48^\circ42'23\overset{''}{.}9053 \pm 3.5$ mas. These positions are offset from one another by $\Delta\alpha = 3.5$ and $\Delta\delta = 5.1$ mas, but despite the total offset of 6.2 mas, still consistent with one another to within $\sim 1\sigma$ (the synthesized beam sizes are 41 × 31 mas and 31 × 26 mas for Epochs 1 and 2, respectively). The uncertainties we quote take into account multiple factors that are summed in quadrature: the statistical uncertainty derived from the shape and size of the synthesized beam normalized by the S/N (ΔRA = 0.3 mas, ΔDec = 0.3 mas for Epoch 1 and ΔRA = 0.4 mas, ΔDec = 0.3 mas for Epoch 2); the statistical uncertainty on the position of the phase calibrator, J2311+4543 (0.10 mas); an estimate of the uncertainty from phase-referencing due to the angular separation between the phase calibrator and target (∼3 mas; Kirsten et al. 2015); an estimate of the frequency-dependent shift in the phase calibrator position from the International Celestial Reference Frame (ICRF), here conservatively ∼1 mas (Plavin et al. 2022); and the statistical uncertainty on the positions of the interferometric check sources (1.06 and 1.47 mas for Epochs 1 and 2, respectively). A more in-depth per epoch analysis is presented in Appendix B1.

The final ICRF position of FRB 20220912A is:
RA (J2000) = $23^{\rm h}09^{\rm m}04\overset{\rm s}{.}8989$; ΔRA = 5 mas,
Dec. (J2000) = $48^\circ42'23\overset{''}{.}9078$; ΔDec = 5 mas.

This position is the numerical average of the per epoch positions, and the uncertainties are (conservatively) the quadrature sum of the per epoch uncertainties. The averaging approach was preferred over combining visibilities across epochs, since the magnitude of the positional offset of the check source from its catalogued position differed between Epochs 1 and 2. This suggests some residual systematics (on the order of a milliarcsecond) that remain even after our meticulous calibration, and which might also be evident from the S/N of the combined image in the right most panel of Fig. 3. We have,

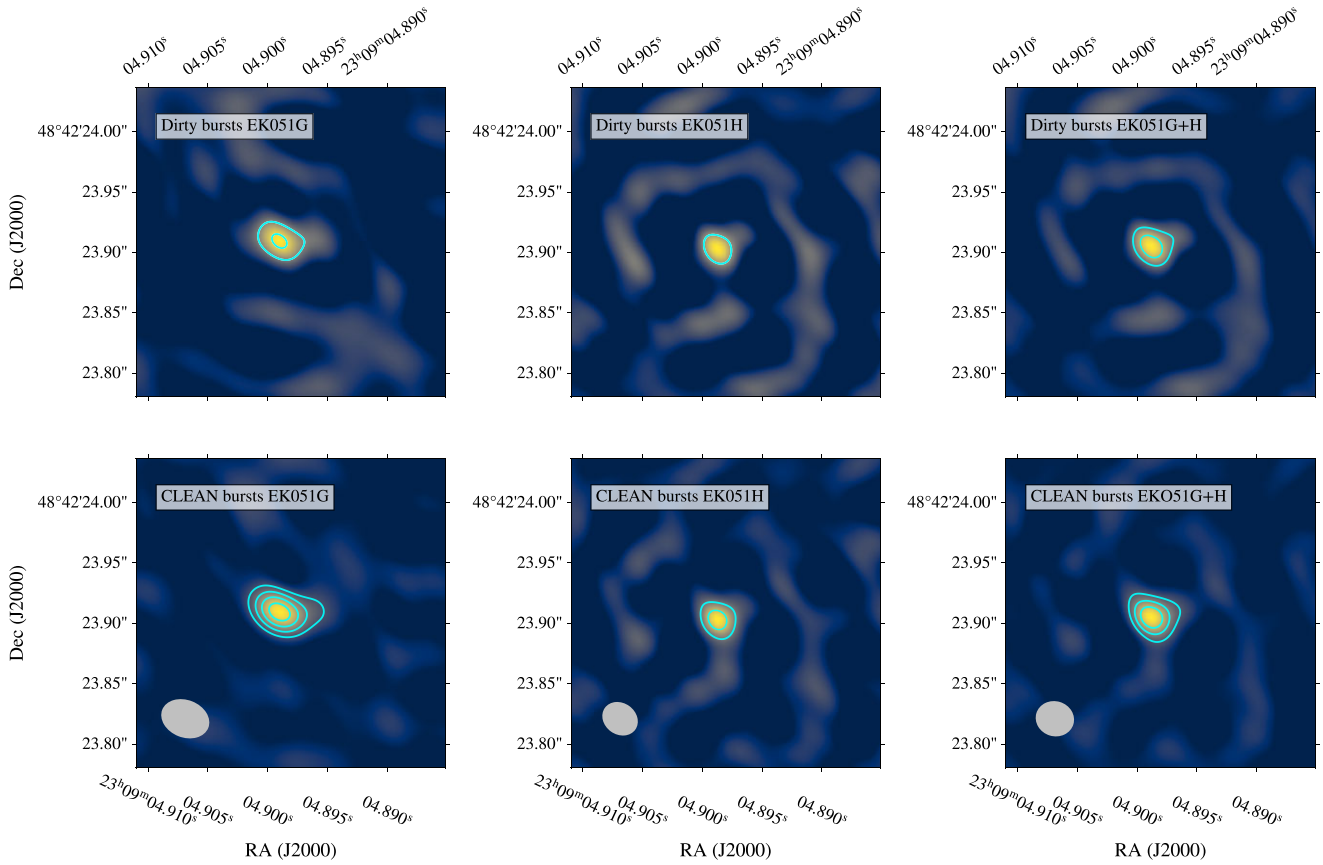

Figure 3. In the top row, the dirty maps of the EVN 1.4 GHz observation of the combined visibilities of the 45 bursts detected in Epoch 1 and 105 bursts detected Epoch 2 are shown in the left and middle panels, respectively. The combined visibilities of both epochs, i.e. all 150 bursts, are shown on the right. The contours start at 4 times the RMS noise level of each image and increase by factors of 3. In the bottom row, the CLEAN images are shown with the synthesized beam displayed as an ellipse in the bottom left corner.

however, accounted for this in our calculation of the uncertainty on the FRB position.

3.4 Continuum imaging

We also imaged a $2 \times 2\,\mathrm{arcsec}^2$ area surrounding the position of the bursts to search for a compact radio continuum counterpart (i.e. a PRS). Fig. 4 shows these dirty images. The images of the first and second epochs have an RMS of 21 and 24 μJy beam^{-1}, respectively, while the combined data from both epochs have an RMS of 16 μJy beam^{-1}. We find no evidence for any persistent radio emission on milliarcsecond scales, ruling out the presence of a PRS with 5σ upper limits of 105, 120, and 80 μJy for Epochs 1, 2 and the combined map, respectively, in a region of $\sim 2 \times 2\,\mathrm{arcsec}^2$ surrounding FRB 20220912A. Conservatively, using the Epoch 2 map limit, this corresponds to luminosity limit of $L \approx (\mathrm{D}/362.4\,\mathrm{Mpc})^2\, 1.8 \times 10^{28}\,\mathrm{erg\,s^{-1}\,Hz^{-1}}$.

3.5 Burst properties

For each burst, we used DIGIFIL to create filterbank files from the baseband data recorded by Effelsberg. The time and frequency resolution of these filterbanks were 64 μs and 62.5 kHz, respectively. The bursts were then incoherently dedispersed to a DM of 219.37 pc cm^{-3}. This DM value was determined by temporally aligning high S/N, broad-band microshots in the dynamic spectra of exceptionally bright bursts detected from FRB 20220912A with the Nançay Radio Telescope (Hewitt et al. 2023). Optimizing for structure by using `DM_phase` (Seymour, Michilli & Pleunis 2019), with a bandpass filter on the fluctuation frequencies, yields similar results. Since we did not apply coherent dedispersion, we chose enough frequency channels to limit DM smearing in the lowest frequency channel to less than the time resolution of the data. After bandpass correction (subtracting the mean and dividing by the standard deviation of the off-burst noise on a per-channel basis) we applied a static mask at frequencies ranging from 1448–1477 MHz, in addition to manually flagging channels that are contaminated by RFI.

Using the function `curve_fit` from the PYTHON package SCIPY, we fit a one-dimensional Gaussian function to the frequency-averaged light curve of each burst (only considering the spectral extent of the burst which was manually determined). We define the width of a burst as the full width at half-maximum (FWHM) of this Gaussian fit. To calculate the fluence of the burst, we first normalized the light curve and then integrated over the 3σ extent of the one-dimensional Gaussian fit, before multiplying with the radiometer equation (Cordes & McLaughlin 2003). As is convention for Effelsberg observations, we assume a system temperature and gain of 20 K and 1.54 K Jy^{-1}, respectively. These values have an uncertainty of approximately 20 per cent, which propagates into the following energy calculations. We calculated the spectral energy

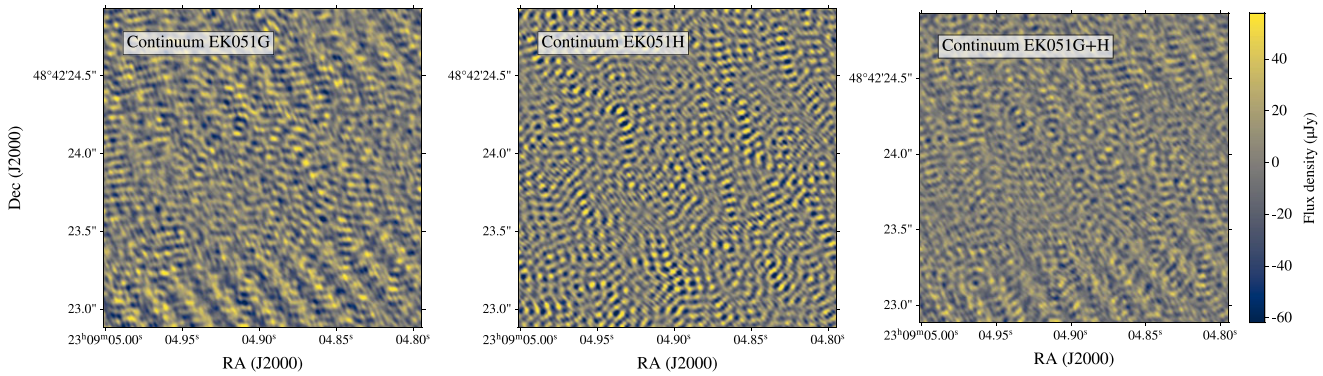

Figure 4. The dirty maps (roughly speaking, the inverse Fourier transform of the calibrated visibilities) of the EVN 1.4 GHz observation of the $\sim 2 \times 2$ arcsec^2 field surrounding FRB 20220912A. We find no peak above 5σ in these maps, resulting in 5σ upper limits of 105, 120, and 80 μJy on the Epochs 1 and 2, and combined maps, respectively. This corresponds to a 5σ upper limit of $L \approx 1.8 \times 10^{28}$erg s^{-1} Hz^{-1} on the brightness of a non-detectable PRS (conservatively using the Epoch 2 map and luminosity distance of 362.4 Mpc). The colour map is scaled to the dynamic range in the combined map.

density (E_ν) as:

$$E_\nu = \frac{4\pi F \Delta\nu D_L^2}{\nu(1+z)}, \quad (1)$$

where F is the fluence, $\Delta\nu$ is the spectral extent of the burst, ν is central observing frequency, and D_L and z are the luminosity distance (362.4 Mpc) and redshift (0.0771) of the host galaxy of FRB 20220912A, respectively (Ravi et al. 2023).

These properties, as well as the times of arrival of the bursts, are tabulated in Table A1. Fig. 5 shows the normalized distribution of these properties, per epoch. The burst property distributions show little variation between the two epochs. Note that the spectral extent of the burst only considers the observed range, and is consequently often a lower limit as many bursts appear to have emission outside of our observing window. In these cases, the burst fluences are thus also lower limits. The median values for width and fluence of all bursts detected are 6.6 ms and 47 Jy ms, respectively.

4 DISCUSSION AND CONCLUSIONS

In this paper, we report the detection of 150 bursts from FRB 20220912A using an ad hoc EVN-Lite array of dishes, which allowed us to localize this FRB source to a precision of a few milliarcsecond: RA (J2000) = 23^{h}09^{m}04^s.8988 ± 5 mas, Dec. (J2000) = 48°42′23″.9078 ± 5 mas. FRB 20220912A is now the sixth repeating FRB source to be localized to milliarcsecond precision using VLBI. We find that FRB 20220912A is significantly closer to the optical centre of its host galaxy, PSO J347.2702+48.70, compared to the earlier localization presented by Ravi et al. (2023), shown in Fig. 6. The transverse offset from the host galaxy centre is ≈0.8 kpc. The precision of this VLBI localization corresponds to a physical length of less than 10 pc at the redshift of the source, and this mas-level position will serve future high-resolution IR/optical/UV imaging with *HST*, *JWST*, and the Extremely Large Telescope (ELT), which could reveal star-forming regions or other discrete sources coincident on parsec scales with the position of FRB 20220912A.

FRB 20121102A and FRB 20190520B are the only known repeating FRBs that exhibit a compact PRS (Marcote et al. 2017; Niu et al. 2022), which may represent a hyper-nebula powered by the burst source (e.g. Sridhar & Metzger 2022). These are also two of the four repeaters from which burst storms have been observed (e.g. Li et al. 2021; Hewitt et al. 2022; Niu et al. 2022; Jahns et al. 2023), the other two being FRB 20200120E (Nimmo et al. 2023) and FRB 20201124A (e.g. Lanman et al. 2022; Zhou et al. 2022).

The upper limit we have placed on the presence of a PRS for FRB 20220912A is more than an order of magnitude below the luminosity of the PRSs associated with FRB 20121102A and FRB 20190520B, ruling out a source of this nature. Alternatively, a low-luminosity PRS ($\sim 5 \times 10^{27}$erg s^{-1} Hz^{-1}; Bruni et al. 2023), would be more than a factor of three fainter than our upper limit and undetectable (assuming a flat spectral index).

There exists a catalogued continuum radio source, APTF J230904+484222, detected by the Westerbork Synthesis Radio Telescope Aperture Tile In Focus (WSRT-APERTIF) and located at RA (J2000) = 23^{h}09^{m}04^s.9 ± 1.7 arcsec, Dec. (J2000) = 48°42′22″.3 ± 2.2 arcsec (Kutkin et al. 2022), which is 1.6 arcsec away from our VLBI position for FRB 20220912A . APTF J230904+484222 has a peak brightness of 0.27 ± 0.04 mJy beam^{-1} at 1355 MHz, corresponding to a luminosity of L ≈(D/362.4 Mpc)^2 3.9 × 10^{28}erg s^{-1} Hz^{-1} if at the distance of FRB 20220912A. The contours and centroid of this source are overplotted on the optical image and VLBI position in Fig. 6. The centroid position does not coincide with the nucleus of the galaxy. We also explore 4 × 4 arcsec^2 around this centroid-position for a compact PRS, but the highest peak we find is 0.072 mJy ($<5\sigma$), still more than 3 times fainter than APTF J230904+484222. This continuum radio source thus likely reflects star formation in the host galaxy, similar to the case of FRB 20201124A (Nimmo et al. 2022). Using the 1.4 GHz luminosity-to-SFR relation (Murphy et al. 2011), a star-formation rate of about 2.5 M$_\odot$ yr^{-1} is required to explain the observed radio flux density of APTF J230904+484222. This radio luminosity inferred SFR is consistent with the SFR of $\gtrsim$0.1 M$_\odot$ yr^{-1} derived from Hα observations and is ∼3.5 times less than the star formation rate inferred from radio observations of the host of FRB 20201124A (Dong et al. 2024).

If the PRSs associated with FRB 20121102A and FRB 20190520B are in fact hyper-nebulae, powered by the central active magnetar (Sridhar & Metzger 2022), the lack of a PRS in the case of FRB 20220912A is particularly surprising, given how active this source is. The absence of a PRS is, however, consistent with the stable and near-zero RM that suggests a non-turbulent and clean local environment (e.g. Feng et al. 2023).

We strongly encourage multiwavelength observations of FRB sources that are outliers in terms of proximity or activity, such as

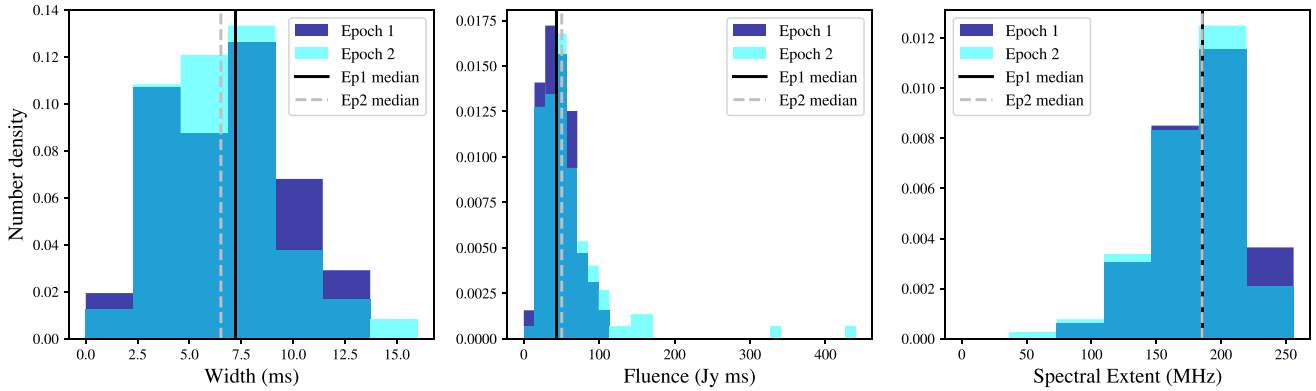

Figure 5. The distribution of the temporal width, fluence, and spectral extent of the bursts we detected are shown in dark blue and cyan for Epochs 1 and 2, respectively. Note that the spectral extent distribution only reflects the observed spectral extent of bursts, which are in many cases lower limits. In these instances the fluences also only reflect lower limits. The histograms have been normalized for each observation, so that the total area equals 1. Vertical lines indicate median values: solid black for Epoch 1 and dashed grey for Epoch 2.

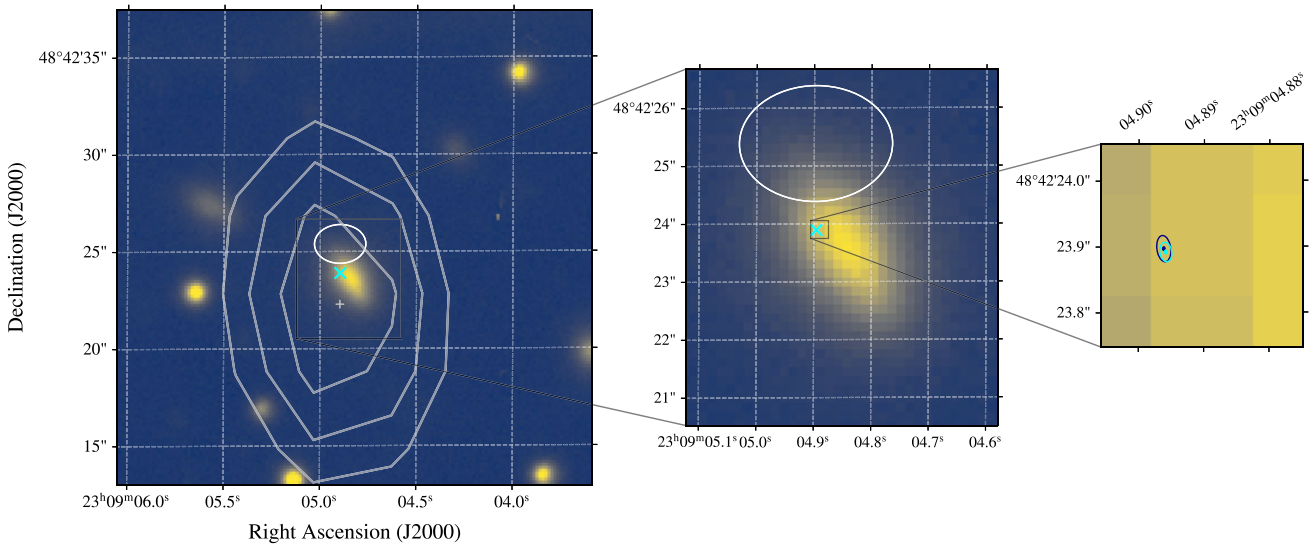

Figure 6. Adapted from Ravi et al. (2023), the background image is the deep optical image (*R* band, obtained with Keck II/ESI; limiting magnitude R∼26) of the host galaxy of FRB 20220912A, PSO J347.2702+48.7066. The grey plus-sign indicates the centroid of the catalogued radio continuum source, APTF J230904+484222, while the grey contours of this source are at levels of 0.16, 0.20, and 0.24 mJy. The approximate 90 per cent error ellipse of the DSA-110 localization of FRB 20220912A is overplotted in white, while our EVN position is indicated by the cyan cross. Note, that the uncertainty on our VLBI position is much smaller than the symbol size and the resolution of the optical image. The insets show consecutive zoom-ins on the EVN position of FRB 20220912A. In the right most inset, the synthesized beams of the observations EK051G and EK051H are overplotted as dark blue and cyan ellipses, respectively, centred at the positions found by combining the visibilities of the bursts on a per epoch basis (see Section 3.3). The solid points at the centre of the ellipses are roughly the size of 90 per cent error regions.

FRB 20220912A and the others FRBs that have been localized to milliarcsecond precision. These observations can be a powerful means of characterizing the local environments of FRBs, and detailed studies such as these complement studies that provide less detailed information for a larger number of sources. Currently, with *HST* it is possible to compare positions at the ∼10 mas level (∼10 per cent of the point spread function width), so there remains much to be gained from precision localizations. Scheduled to commence observations within a decade, the ELT will provide 5 mas resolution, enabling an even stronger optical synergy to milliarcsecond localizations in the radio regime.

ACKNOWLEDGEMENTS

We thank the referee of this manuscript for their thoughtful comments. The authors would also like to extend their gratitude towards Vikram Ravi for sharing the optical image used in Fig. 6. We thank the directors and staff at the various participating antenna stations for allowing us to use their facilities and running the observations. The European VLBI Network (EVN) is a joint facility of independent European, African, Asian, and North American radio astronomy institutes. Scientific results from data presented in this publication are derived from EVN project code EK051. Research by the AstroFlash group at the University of Amsterdam, ASTRON, and JIVE is supported in part by Dutch Research Council (NWO) Vici grant (PI: Hessels; VI.C.192.045). SB was supported by an NWO Veni

fellowship (VI.Veni.212.058). BM acknowledges financial support from the State Agency for Research of the Spanish Ministry of Science and Innovation under grant nos PID2019-105510GB-C31/AEI/10.13039/501100011033, and PID2022-136828NB-C41 and through the Unit of Excellence María de Maeztu 2020-2023 award to the Institute of Cosmos Sciences (CEX2019-00918-M). FK acknowledges support from Onsala Space Observatory for the provisioning of its facilities/observational support. MB is a McWilliams fellow and an International Astronomical Union Gruber fellow. MB also receives support from the McWilliams seed grant. The Onsala Space Observatory national research infrastructure is funded through Swedish Research Council grant no. 2017–00648. e-MERLIN is a National Facility operated by the University of Manchester at Jodrell Bank Observatory on behalf of STFC, part of UK Research and Innovation. The Medicina and Noto radio telescopes are funded by the Italian Ministry of University and Research (MUR) and are operated as a National Facility by the National Institute for Astrophysics (INAF). Part of the research activities described in this paper were carried out with the contribution of the NextGenerationEU funds within the National Recovery and Resilience Plan (PNRR), Mission 4 – Education and Research, Component 2 – From Research to Business (M4C2), Investment Line 3.1– Strengthening and Creation of Research Infrastructures, Project IR0000026 – Next Generation Croce del Nord. This work is based in part on observations carried out using the 32-m radio telescope operated by the Institute of Astronomy of the Nicolaus Copernicus University in Toruń (Poland) and supported by a Polish Ministry of Science and Higher Education SpUB grant. This project has received funding from the European Union's Horizon 2020 research and innovation programme under grant agreements 730562 (RadioNet) and 101004719 (OPTICON-RadioNet Pilot).

DATA AVAILABILITY

The EVN observations are available on the EVN Data Archive at JIVE[9] under project codes EK051G and EK051H. The relevant code and data products for this work will be uploaded on Zenodo (DOI: 10.5281/zenodo.10622870) at the time of publication.

REFERENCES

Agarwal D. et al., 2020, MNRAS, 497, 1661
Bassa C. G. et al., 2017, ApJ, 843, L8
Bhandari S. et al., 2023, ApJ, 958, L19
Bhardwaj M. et al., 2021, ApJ, 910, L18
Bhardwaj M. et al., 2023, preprint (arXiv:2310.10018)
Bochenek C. D. et al., 2020, Nature, 587, 59
Bruni G. et al., 2023, preprint (arXiv:2312.15296)
Chatterjee S. et al., 2017, Nature, 541, 58
CHIME/FRB Collaboration 2018, ApJ, 863, 48
Chime/Frb Collaboration 2020, Nature, 582, 351
CHIME/FRB Collaboration 2020, Nature, 587, 54
Chime/Frb Collaboration 2023, ApJ, 947, 83
Cordes J. M., Lazio T. J. W., 2002, preprint (astro–ph/0207156)
Cordes J. M., McLaughlin M. A., 2003, ApJ, 596, 1142
Day C. K. et al., 2021, Astron. Telegram, 14515, 1
Dong Y. et al., 2024, ApJ, 961, 44
Eftekhari T., Berger E., 2017, ApJ, 849, 162
Feng Y. et al., 2023, preprint (arXiv:2304.14671)
Gordon A. C. et al., 2023, ApJ, 954, 80
Greisen E. W., 2003, in Heck A., ed., Astrophysics and Space Science Library Vol. 285, Information Handling in Astronomy – Historical Vistas. Kluwer Academic Publishers, Dordrecht, p. 109
Hewitt D. M. et al., 2022, MNRAS, 515, 3577
Hewitt D. M. et al., 2023, MNRAS, 526, 2039
Jahns J. N. et al., 2023, MNRAS, 519, 666
Keimpema A. et al., 2015, Exp. Astron., 39, 259
Kirsten F. et al., 2022a, Nature, 602, 585
Kirsten F. et al., 2022b, Astron. Telegram, 15727, 1
Kirsten F. et al., 2021, Nat. Astron., 5, 414
Kirsten F. et al., 2015, A&A, 577, A111
Kremer K., Piro A. L., Li D., 2021, ApJ, 917, L11
Kutkin A.M. et al., 2022, A&A, 667,A39
Lanman A. E. et al., 2022, ApJ, 927, 59
Law C. et al., 2021, Astron. Telegram, 14526, 1
Li D. et al., 2021, Nature, 598, 267
Mannings A. G. et al., 2021, ApJ, 917, 75
Marcote B. et al., 2017, ApJ, 834, L8
Marcote B. et al., 2020, Nature, 577, 190
McKinven R., Chime/Frb Collaboration, 2022, Astron. Telegram, 15679, 1
McMullin J. P., Waters B., Schiebel D., Young W., Golap K., 2007, in Shaw R. A., Hill F., Bell D. J.eds, ASP Conf. Ser. Vol. 376, Astronomical Data Analysis Software and Systems XVI. Astron. Soc. Pac., San Francisco, p. 127
Metzger B. D., Margalit B., Sironi L., 2019, MNRAS, 485, 4091
Michilli D. et al., 2018, Nature, 553, 182
Murphy E. J. et al., 2011, ApJ, 737, 67
Nimmo K. et al., 2021, Nat. Astron., 5, 594
Nimmo K. et al., 2022, ApJ, 927, L3
Nimmo K. et al., 2023, MNRAS, 520, 2281
Niu C. H. et al., 2022, Nature, 606, 873
Petroff E., Hessels J. W. T., Lorimer D. R., 2022, A&A Rev., 30, 2
Piro L. et al., 2021, A&A, 656, L15
Plavin A. et al., 2022, MNRAS, 511, 6033
Pleunis Z. et al., 2021, ApJ, 923, 1
Ravi V. et al., 2022, MNRAS, 513, 982
Ravi V. et al., 2023, ApJ, 949, L3
Ravi V., 2019, Nat. Astron., 3, 928
Ravi V., 2022, Astron. Telegram, 15693, 1
Ricci R. et al., 2021, Astron. Telegram, 14549, 1
Seymour A., Michilli D., Pleunis Z., 2019, Astrophysics Source Code Library, record ascl:1910.004
Sharma K. et al., 2023, ApJ, 950, 175
Shepherd M. C., Pearson T. J., Taylor G. B., 1994, BAAS, 26, 987
Snelders M. P. et al., 2023, Nat. Astron., 7, 1486
Spitler L. G. et al., 2016, Nature, 531, 202
Sridhar N., Metzger B. D., 2022, ApJ, 937, 5
Tendulkar S. P. et al., 2017, ApJ, 834, L7
Tendulkar S. P. et al., 2021, ApJ, 908, L12
van Bemmel I. M. et al., 2022, PASP, 134, 114502
van Straten W., Bailes M., 2011, PASA, 28, 1
Wharton R. et al., 2021a, Astron. Telegram, 14529, 1
Wharton R. et al., 2021b, Astron. Telegram, 14538, 1
Whitney A., Kettenis M., Phillips C., Sekido M., 2010, in Navarro R., Rogstad S., Goodhart C. E., Sigman E., Soriano M., Wang D., White L. A., Jacobs C. S., eds, Sixth International VLBI Service for Geodesy and Astronomy. Proceedings from the 2010 General Meeting. p. 192, VLBI2010: From Vision to Reality". Held 7-13 February, 2010 in Hobart, Tasmania, Australia. Edited by D. Behrend and K.D. Baver. NASA/CP 2010-215864.
Zhang Y.-K. et al., 2023, ApJ, 955, 142
Zhou D. J. et al., 2022, Res. Astron. Astrophys., 22, 124001

APPENDIX A: BURST PROPERTIES

Properties of the bursts detected in our PRECISE observations are reported in Table A1.

[9] http://archive.jive.nl/

Table A1. Burst properties.

Burst ID	MJD[a]	Temporal width (ms)[b]	Fluence (Jy ms)[c, d]	Spectral energy density (10^{29} erg Hz^{-1})[d]
G001	59874.01351809	4.4 ± 0.5	29	4.0
G002	59874.01727595	7.4 ± 0.7	31	7.3
G003	59874.01747271	7.2 ± 0.3	68	13.2
G004	59874.01793008	12.2 ± 0.8	61	14.6
G005	59874.01811878	0.99 ± 0.03	45	9.3
G006	59874.02032330	2.8 ± 0.1	64	13.6
G007	59874.02489297	4.5 ± 0.5	25	4.7
G008	59874.02843250	9.8 ± 1.2	31	5.3
G009	59874.03745237	9.7 ± 0.7	51	11.8
G010	59874.03786912	8.6 ± 1.0	38	4.1
G011	59874.03875683	4.4 ± 0.8	13	2.9
G012	59874.04316232	4.1 ± 0.4	22	4.0
G013	59874.04664155	4.2 ± 0.5	20	4.9
G014	59874.05413382	6.4 ± 0.6	32	6.5
G015	59874.06219702	4.7 ± 0.1	89	17.7
G016	59874.06233498	5.6 ± 0.4	44	6.9
G017	59874.06245408	12.1 ± 0.7	68	15.1
G018	59874.06263542	6.5 ± 0.6	31	6.2
G019	59874.06968019	13.4 ± 1.2	47	9.6
G020	59874.07035018	7.6 ± 0.4	52	10.8
G021	59874.07224331	5.3 ± 0.5	25	5.6
G022	59874.07548403	8.2 ± 0.8	37	5.9
G023	59874.08625452	7.6 ± 1.2	17	3.8
G024	59874.08928933	7.8 ± 0.4	62	13.5
G025	59874.09349927	4.0 ± 0.4	23	4.9
G026	59874.09427777	10.0 ± 0.7	61	11.7
G027	59874.09637159	3.6 ± 0.3	31	5.6
G028	59874.09921041	7.3 ± 0.7	28	6.6
G029	59874.09978949	4.3 ± 0.2	46	9.5
G030	59874.10045871	9.8 ± 0.8	43	8.8
G031	59874.10747114	7.5 ± 0.9	23	5.6
G032	59874.11355427	7.2 ± 0.3	102	18.6
G033	59874.11922025	6.5 ± 0.5	46	8.0
G034	59874.11991756	3.9 ± 0.2	64	11.5
G035	59874.12232641	5.3 ± 0.5	30	5.0
G036	59874.12390893	8.0 ± 0.5	48	11.6
G037	59874.13620542	8.5 ± 0.6	50	9.8
G038	59874.14528686	9.4 ± 0.5	78	11.3
G039	59874.15568159	6.1 ± 0.7	33	5.0
G040	59874.16142370	9.9 ± 0.5	73	12.4
G041	59874.16178252	4.0 ± 0.2	67	8.9
G042	59874.16582486	2.2 ± 0.2	21	2.5
G043	59874.18358549	11.1 ± 0.5	97	16.4
G044	59874.18760978	8.5 ± 0.4	78	14.0
G045	59874.19445752	5.4 ± 0.4	38	6.8
H001	59876.88324165	6.0 ± 0.4	40	7.2
H002	59876.88367760	2.6 ± 0.1	47	10.4
H003	59876.89137390	5.3 ± 0.4	44	7.3
H004	59876.89478408	4.0 ± 0.1	76	14.6
H005	59876.89971573	11.9 ± 0.5	102	21.1
H006	59876.89978801	4.3 ± 0.1	79	15.6
H007	59876.90039785	11.1 ± 0.4	117	25.4
H008	59876.90169720	4.5 ± 0.1	101	21.5
H009	59876.90958331	5.7 ± 0.2	94	22.6
H010	59876.91101023	5.7 ± 0.3	58	9.8
H011	59876.91463753	10.3 ± 0.4	88	21.1
H012	59876.91553057	12.3 ± 0.3	136	32.5
H013	59876.91577982	6.0 ± 0.2	79	16.3
H014	59876.91658368	7.6 ± 0.1	167	37.1
H015	59876.92139371	0.62 ± 0.04	16	3.0
H016	59876.92613409	3.7 ± 0.3	29	4.5
H017	59876.92625989	5.9 ± 0.5	35	7.7
H018	59876.92762306	4.2 ± 0.3	37	5.9

Table A1 – *continued*

Burst ID	MJD[a]	Temporal width (ms)[b]	Fluence (Jy ms)[c, d]	Spectral energy density (10^{29} erg Hz^{-1})[d]
H019	59876.93432863	2.0 ± 0.3	12	2.0
H020	59876.94064355	5.0 ± 0.1	111	21.3
H021	59876.94137123	9.6 ± 0.3	147	25.8
H022	59876.94460382	7.9 ± 0.5	60	8.9
H023	59876.94530712	4.3 ± 0.3	44	8.4
H024	59876.94593990	10.6 ± 0.3	164	37.8
H025	59876.94619106	4.2 ± 0.6	20	3.1
H026	59876.94633808	7.1 ± 0.4	68	12.7
H027	59876.94734039	10.4 ± 0.4	111	17.3
H028	59876.95002759	4.7 ± 0.5	27	5.1
H029	59876.95047486	5.0 ± 0.6	20	3.9
H030	59876.95165196	3.7 ± 0.1	330	75.7
H031	59876.95273572	6.2 ± 0.4	43	7.7
H032	59876.96054167	4.2 ± 0.3	33	7.4
H033	59876.96082704	7.9 ± 0.7	40	7.8
H034	59876.96142198	7.6 ± 0.5	46	9.4
H035	59876.96154518	9.1 ± 0.4	77	15.3
H036	59876.96356728	6.1 ± 0.3	64	14.4
H037	59876.96613912	6.8 ± 0.3	79	16.7
H038	59876.96640209	3.9 ± 0.1	89	18.7
H039	59876.96936874	5.1 ± 0.3	52	11.1
H040	59876.97106987	8.5 ± 1.2	29	3.6
H041	59876.97160880	7.7 ± 0.4	62	13.5
H042	59876.97435577	9.0 ± 0.5	56	12.4
H043	59876.97603178	6.6 ± 0.3	59	13.5
H044	59876.97648147	5.6 ± 0.2	72	12.1
H045	59876.98304796	4.8 ± 0.3	34	7.4
H046	59876.98323034	4.5 ± 0.2	52	10.6
H047	59876.98348756	4.3 ± 0.2	71	16.3
H048	59876.98513941	34.0 ± 0.2	54	11.1
H049	59876.98526088	9.6 ± 1.1	31	6.3
H050	59876.98593060	5.1 ± 0.4	28	6.8
H051	59876.98819198	4.0 ± 0.4	25	4.7
H052	59876.99315217	8.3 ± 0.5	61	11.0
H053	59876.99340664	9.5 ± 1.2	27	5.5
H054	59876.99357744	6.9 ± 0.3	57	13.7
H055	59876.99559429	8.8 ± 0.6	49	9.7
H056	59876.99899468	4.4 ± 0.5	25	4.2
H057	59876.99935655	10.6 ± 0.8	54	12.4
H058	59876.99984536	7.7 ± 0.5	70	7.3
H059	59877.00043210	7.8 ± 0.8	37	6.1
H060	59877.00097951	8.8 ± 0.6	52	8.0
H061	59877.00835109	5.6 ± 0.4	43	7.1
H062	59877.00893303	4.5 ± 0.3	34	7.4
H063	59877.00906912	8.2 ± 1.3	21	3.6
H064	59877.00966560	4.6 ± 0.2	67	13.9
H065	59877.01003499	7.3 ± 0.4	53	11.7
H066	59877.01018686	5.1 ± 0.3	45	7.9
H067	59877.01205399	6.6 ± 0.9	26	3.7
H068	59877.01214328	4.7 ± 0.5	23	4.1
H069	59877.01324536	6.9 ± 0.5	40	7.9
H070	59877.01413124	7.0 ± 0.2	98	21.1
H071	59877.01801725	8.2 ± 0.5	50	8.7
H072	59877.02245511	3.3 ± 0.5	22	1.8
H073	59877.02286325	1.4 ± 0.1	19	4.6
H074	59877.03150464	9.7 ± 0.4	94	20.5
H075	59877.03195097	7.4 ± 0.8	44	5.1
H076	59877.03314940	4.4 ± 0.3	41	8.2
H077	59877.03426822	6.9 ± 0.8	29	5.7
H078	59877.03454198	8.0 ± 0.5	51	11.4
H079	59877.03641293	4.4 ± 0.6	20	2.8
H080	59877.03723562	7.6 ± 0.7	43	5.2
H081	59877.03799905	8.3 ± 0.3	79	19.0

Table A1 – *continued*

Burst ID	MJD[a]	Temporal width (ms)[b]	Fluence (Jy ms)[c, d]	Spectral energy density (10^{29} erg Hz^{-1})[d]
H082	59877.03815510	6.5 ± 0.6	41	6.0
H083	59877.04259124	15.2 ± 0.2	429	102.8
H084	59877.0443353	4.4 ± 0.6	23	3.1
H085	59877.04472092	7.3 ± 0.5	53	9.2
H086	59877.04932255	6.6 ± 0.4	52	8.9
H087	59877.04953494	7.3 ± 0.5	44	8.0
H088	59877.05595215	7.1 ± 0.9	29	4.2
H089	59877.05718630	15.7 ± 1.4	54	9.5
H090	59877.05994232	3.6 ± 0.5	19	2.9
H091	59877.06011452	7.8 ± 0.4	68	15.4
H092	59877.06108046	12.4 ± 0.4	150	33.2
H093	59877.06118988	3.5 ± 0.5	17	3.3
H094	59877.06124699	4.0 ± 0.2	58	11.3
H095	59877.06140918	11.9 ± 1.1	43	8.2
H096	59877.06188390	6.5 ± 0.7	32	5.1
H097	59877.06229430	4.9 ± 0.4	38	7.4
H098	59877.06460628	8.4 ± 0.5	53	11.6
H099	59877.06650560	2.7 ± 0.3	39	1.8
H100	59877.06930657	9.0 ± 0.3	99	20.7
H101	59877.07478215	7.2 ± 0.6	64	5.2
H102	59877.07574649	4.8 ± 0.2	77	17.6
H103	59877.07668063	4.9 ± 0.5	28	4.2
H104	59877.07901416	7.4 ± 0.5	48	11.0
H105	59877.07957926	6.1 ± 0.7	28	4.0

Notes.[a]The time-of-arrival of the burst at the Solar system barycentre in TDB, corrected to infinite frequency for a DM of 219.37 pc cm^{-3} and using a DM constant of 1/(2.41 × 10^{-4}) MHz^2 pc^{-1} cm^3 s.
[b]FWHM of one-dimensional Gaussian fit.
[c]Measured over the spectral extent of the burst.
[d]The estimated uncertainty is approximately 20 per cent due to uncertainty in the system equivalent flux density (SEFD).

APPENDIX B: INDIVIDUAL BURST LOCALIZATION ACCURACY

B1 Per Epoch analysis

Marcote et al. (2017) and Nimmo et al. (2022) investigated the astrometry of single burst localizations. Here, we undertake a similar analysis. Fig. B1 shows the peak position of the dirty maps of individual bursts overplotted on the dirty map of the combined visibilities of the 45 bursts in Epoch 1 and 105 bursts in Epoch 2. The data points have been coloured according to a detection metric that is defined as fluence of the burst divided by the square root of the temporal width (which we define as the FWHM of a Gaussian fit) of the burst (Marcote et al. 2017). For the sake of brevity in the remainder of the discussion, when referring to the peak position of the dirty map of an individual burst, we will simply call it the individual peak positions. We observe that the individual peak positions are scattered around the best position (found by combining the visibilities of all bursts for an epoch). The offset between the individual peak positions and the best position can be as much as a few hundred milliarcseconds. We note that using the peak position of the dirty maps of a single burst to determine the localization region is not ideal. As discussed in Nimmo et al. (2022), the peak levels of the side lobes in the dirty maps are on average > 97 per cent and in particularly bad cases where the bursts are faint and *uv*-coverage is poor it can be even higher than the main lobe. While brighter bursts that have a higher detection metric tend to have smaller offsets, the relation is not a simple linear one. Since the spectral extent of bursts differ, and the number of baselines differs for different parts of our observing band (see Fig. 1), the *uv*-coverage is dependent on where the burst falls within our observing frequency range. A narrow-band burst at the edges of our observing window might thus partly be observed at spectral ranges where the number of antennas is as few as two, and consequently due to the poor *uv*-coverage have a less accurate localization.

An alternative approach to determining the position of a single burst has been presented in Nimmo et al. (2022). The authors fit the cross-pattern observed in most dirty maps of individual bursts with two two-dimensional Gaussians, and then fit the intersection of these Gaussians with another two-dimensional Gaussian. This method has the advantage of smoothing over the prominent side lobes in these dirty maps, and thus provides a more robust localization region than merely picking the highest peak in the dirty map. Fortunately, we have detected a very large number of bursts from FRB 20220912A throughout our two observations, ensuring sufficient S/N to clearly identify the burst position and so we refrain from applying the aforementioned two-dimensional-Gaussian fit method. Consequently, we do however note that the accuracy and precision of the single burst localizations shown here (peak of the dirty map) are significantly underestimated.

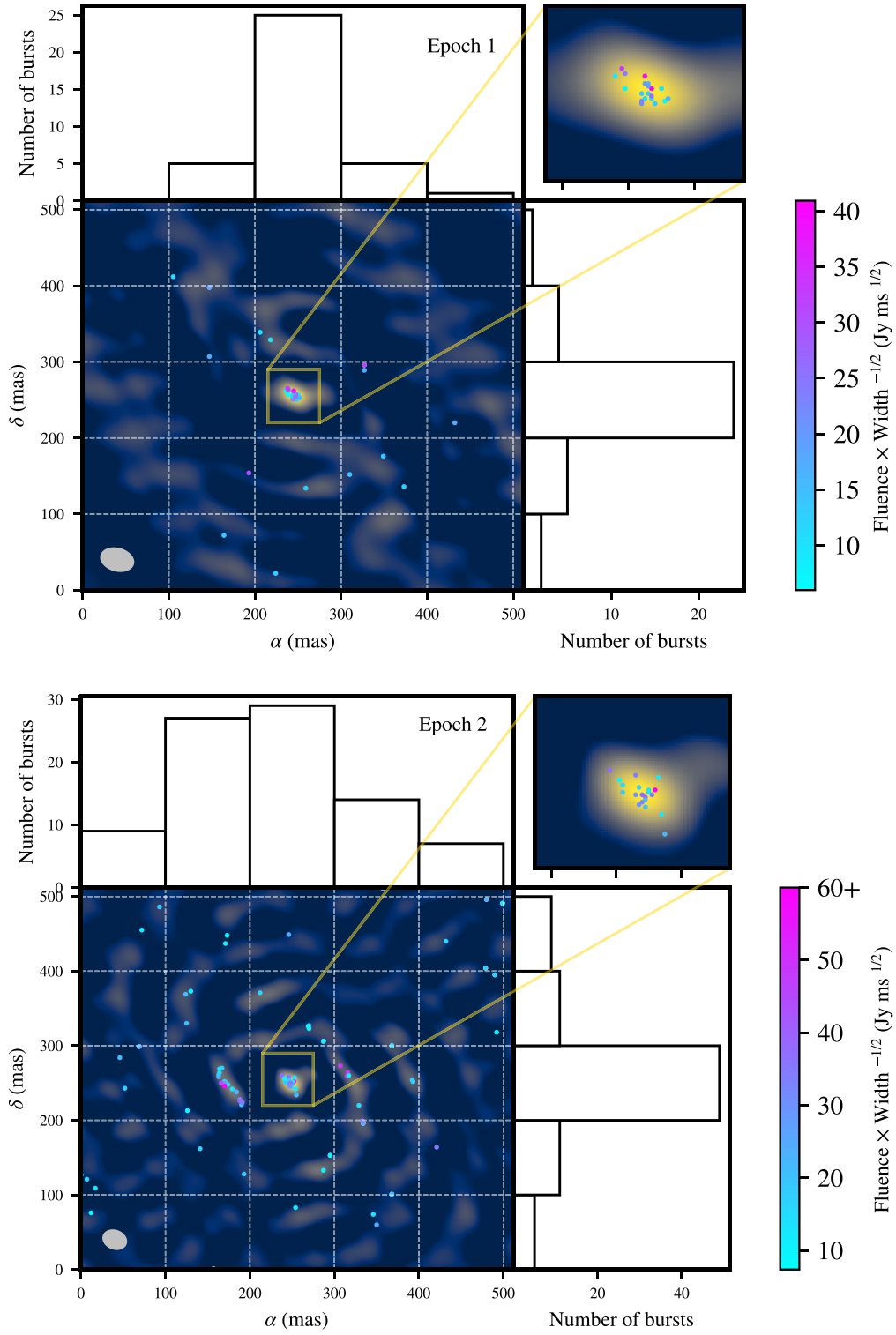

Figure B1. The position of the peak S/N of the dirty maps of individual bursts, compared to the best-known FRB position for Epoch 1 (top) and Epoch 2 (bottom). The points have been coloured according to a detection metric that is defined as fluence of the burst divided by the square root of the temporal width of the burst. The uncertainty of individual burst positions is underestimated, since only the peak value of the dirty map is used here for illustrative purposes. The true uncertainty of individual burst positions is more precisely known from taking into account the side lobes. Bursts that occur during times when the calibration solutions are less robust are excluded from this analysis.

This paper has been typeset from a TEX/LATEX file prepared by the author.